Supplementary Information for
High-pressure elastic properties of dolomite melt supporting carbonate-induced melting in deep upper mantle

Man Xu[1,2], Zhicheng Jing[2*], Suraj K. Bajgain[3], Mainak Mookherjee[3], James A. Van Orman[1],
Tony Yu[4], Yanbin Wang[4]
[1]Department of Earth, Environmental, and Planetary Sciences, Case Western Reserve University,
Cleveland, OH 44106, USA
[2]Department of Earth and Space Sciences, Southern University of Science and Technology,
Shenzhen, Guangdong, 518055, China
[3]Department of Earth, Ocean, and Atmospheric Sciences, Florida State University, Tallahassee,
FL 32306, USA
[4]Center for Advanced Radiation Sources, The University of Chicago, Chicago, IL 60637, USA

This supplementary file includes:

- **Text S1.** Criteria for detecting melting using ultrasonic signals.
- **Text S2**. Data fitting procedure.
- **Text S3**. Calculation of velocity reductions for partially molten assemblages.
- **Text S4**. Comparison with previous results.
- **Fig. S1.** Cell assemblies for the experiments.
- **Fig. S2.** Ultrasonic signals for the sample with increasing temperatures.
- **Fig. S3.** Experimental images for the sink-float experiments.
- **Fig. S4.** SEM results for the sample quenched from ultrasonic experiments.
- **Fig. S5.** Correlations between fitted *K* and *K*' using experimental data.
- **Fig. S6.** FPMD simulation results for the density of dolomite melt.
- **Fig. S7.** Constraint on melt geometry applicable to upper mantle.
- **Fig. S8.** Velocity vs. density plot for dolomite melt.
- **Table S1.** Composition of the quenched samples measured by EDS.
- **Table S2.** Experimentally measured sound velocity data for dolomite melt.

www.pnas.org/cgi/doi/10.1073/pnas.2004347117

- **Table S3.** FPMD simulation data for dolomite melt.
- **References**

Supplementary Text

Text S1. Criteria for detecting melting using ultrasonic signals

With increasing temperature, the pattern of ultrasonic signals changes as the sample transforms from solid to partially molten and then to fully molten liquid (Fig. S2). In the solid state, both P-wave and S-wave signals for the sample (signals reflected at the sample-BP interface) can be clearly observed; whereas in the partially molten state, the S-wave signal completely disappears and the P-wave signal becomes very weak (Fig. S2). Complete melting of the sample is indicated by: (1) reappearance of a clear P-wave signal for the sample; (2) increase in the P-wave signal amplitude compared to the partially molten state; (3) shift of the liquid sample P-wave signal to the right on the time axis compared to the solid sample signal (Fig. S2). After the sample is fully molten, the amplitude of the signals becomes smaller with increasing temperature. All the data reported in this study were measured on the liquid phase when the fully molten state had been achieved. The quenched samples show typical quench textures for carbonate melts (Fig. S4), confirming that samples were fully molten during the experiments.

Text S2. EOS fitting procedure

We fit our experimental data using the third-order isothermal Birch-Murnaghan EOS (1), which is given as

$$P = \frac{3K_{T0}}{2}\left[\left(\frac{\rho}{\rho_0}\right)^{\frac{7}{3}} - \left(\frac{\rho}{\rho_0}\right)^{\frac{5}{3}}\right]\left\{1 + \frac{3}{4}(K_T' - 4)\left[\left(\frac{\rho}{\rho_0}\right)^{\frac{2}{3}} - 1\right]\right\} \quad [1]$$

where P is pressure, K_{T0} the isothermal bulk modulus at room pressure, K_T' the pressure derivative of the bulk modulus, ρ_0 the room-pressure density, and ρ is the high-pressure density. Based on Eulerian finite strain theory, the high-pressure bulk modulus is given as (2)

$$K_T = K_{T0}\left(\frac{\rho}{\rho_0}\right)^{\frac{5}{3}}\left\{1 + \frac{1}{2}\left(1 - \left(\frac{\rho}{\rho_0}\right)^{\frac{2}{3}}\right)\left[5 - 3K_T' - \frac{27}{4}(4 - K_T')\left(1 - \left(\frac{\rho}{\rho_0}\right)^{\frac{2}{3}}\right)\right]\right\}. \quad [2]$$

The room-pressure density (ρ_0) at a temperature T is given as

$$\rho_0 = \rho_{0,T_{ref}} \exp\left[-\alpha(T - T_{ref})\right], \quad [3]$$

where T_{ref} is the reference temperature and is chosen to be 1573 K in this study, and α is the thermal expansion coefficient for dolomite melt. Although the thermal expansion coefficient for dolomite melt has not been directly measured yet, a recent room-pressure experimental study by Hurt & Lange (3) showed that all alkaline-earth carbonate melts have nearly identical thermal expansion coefficient which is 1.64×10^{-4} K^{-1}, and we use this value as a fixed parameter for dolomite melt in this study. The room-pressure bulk modulus (K_{T0}) is also a function of temperature and can be expressed in terms of the Anderson-Grüneisen parameter δ_T (4) as

$$K_{T0} = K_{T0,Tref}\left(\frac{\rho_{0,Tref}}{\rho_0}\right)^{-\delta_T}, \qquad [4]$$

Inserting [4] into [3], we get

$$K_{T0} = K_{T0,Tref}\,exp\left[-\alpha\delta_T\left(T - T_{ref}\right)\right]. \qquad [5]$$

The adiabatic bulk modulus is related to the isothermal bulk modulus through

$$K_S = K_T(1 + \alpha\gamma T), \qquad [6]$$

where γ is the Grüneisen parameter. The Grüneisen parameter for dolomite melt can be estimated from our FPMD simulations, and is 0.8 and 0.7 at room pressure based on GGA and LDA, respectively (Table 1). Although the simulation results show that the Grüneisen parameter increases slightly with pressure for dolomite melt, similar to what has been observed in silicate melts (5, 6), the Grüneisen parameter can be treated as a constant for fitting our experimental data, considering the limited pressure range (<6 GPa). We take the average of the results from GGA and LDA simulations and use 0.75 for the Grüneisen parameter for dolomite melt. A slight change of the Grüneisen parameter does not affect the fitting results significantly. Sound velocity (c) is related to adiabatic bulk modulus (K_S) and density (ρ) through

$$c = \sqrt{K_S/\rho}\ . \qquad [7]$$

We fit our data using a Monte-Carlo approach which can help us better estimate the fitting uncertainties (7). The fitting parameters in this study are $\rho_{0,Tref}$, $K_{T0,Tref}$, K_T' and δ_T. A million sets of parameter values were generated from a random distribution in the parameter space of 2.19-2.42 g/cm^3 for $\rho_{0,1573\,K}$, 5-25 GPa for $K_{T0,1573\,K}$, 3-13 for K_T' and 1-5 for δ_T based on a previous simulation study on dolomite melt (8). For a given set of parameters, we calculated $\rho_{0,i}$ and $K_{T0,i}$ at experimental temperature T_i using Eqns. [3] and [5], and high-pressure density ρ_i and isothermal bulk modulus $K_{T,i}$ can be calculated using Eqns. [1] and [2], respectively, with our experimental pressure data P_i. The calculated $K_{T,i}$ was converted to $K_{S,i}$ using Eqn. [6] and finally the modeled sound velocity c_i^{model} was calculated via Eqn. [7]. The same calculations were repeated for each experimental *P*, *T* condition. As for the high-pressure density, we used the neutral point as an anchor for the EOS curve. The same randomly generated parameter sets as those in velocity data fitting were used to calculate the modeled high-pressure density ρ^{model} at experimental *P* and *T* according to Eqns. [3], [5] and [1]. The fitting was performed simultaneously on both the velocity data and the density data, by minimizing the combined χ^2, which was calculated as

$$\chi^2 = \sum_i \left[\frac{\left(c_i^{data} - c_i^{model}\right)^2}{\left(\sigma_i^c\right)^2} + \frac{\left(\rho^{data} - \rho^{model}\right)^2}{(\sigma^\rho)^2} \right], \qquad [8]$$

where c_i^{data} is the measured sound velocity for experiment i, σ_i^c is the total uncertainty in the sound velocity which is the sum of the uncertainty in the sound velocity measurements and the propagated equivalent uncertainty in sound velocity due to the uncertainty in pressure, ρ^{data} is the measured high-pressure density for the neutral point and σ^ρ is the uncertainty in density measurements including both the uncertainty in density and propagated equivalent uncertainty from pressure. The χ^2 calculations were performed for all of the one million randomly generated parameter sets for $(\rho_0, K_{T0}, K_T', \delta_T)$. The best-fit values for the parameters were those that generated the minimum χ^2.

For the FPMD simulation results, we use the Mie-Grüneisen thermal equation of state to describe the pressure, temperature and volume data obtained for dolomite melt:

$$P\,(V,T) = P\,(V,T_{ref}) + \left(\frac{dP}{dT}\right)_V (T - T_{ref}), \qquad [9]$$

where $\left(\frac{dP}{dT}\right)_V$ is the temperature derivative of pressure at constant density or volume. In Eqn. [9], $P\,(V,T_{ref})$ is the pressure at reference isotherm ($T_{ref} = 2000\,K$). The pressure-volume relationship at the reference temperature is defined by the third-order Birch-Murnaghan equation of state (Eqn. [1]). Other thermodynamic quantities such as the Grüneisen parameter (γ), and the isothermal bulk modulus (K_T) are calculated using the following relations:

$$\gamma = \frac{V}{C_V}\left(\frac{dP}{dT}\right)_V, \qquad [10]$$

$$K_T = -V\left(\frac{dP}{dV}\right)_T, \qquad [11]$$

where $\left(\frac{dP}{dT}\right)_V$ and γ can be expressed as a function of volume or density (Table 1).

Text S3. *Calculation of velocity reductions for partially molten assemblages*

The velocity reductions in *P*- and *S*-wave velocities as a function of melt fraction (*F*) is given as (9, 10)

$$dlnV_p = \frac{dV_p}{V_{p0}} = \frac{V_{p0}-V_p}{V_{p0}} = \left[\frac{\frac{(\beta-1)\Lambda_K}{\Lambda_K+(\beta-1)}+\frac{4}{3}\gamma\Lambda_G}{1+\frac{4}{3}\gamma} - \left(1-\frac{\rho_l}{\rho_s}\right)\right]\frac{F}{2}, \quad [12]$$

$$dlnV_s = \frac{dV_s}{V_{s0}} = \frac{V_{s0}-V_s}{V_{s0}} = \left[\Lambda_G - \left(1-\left(\frac{\rho_l}{\rho_s}\right)\right)\right]\frac{F}{2}, \quad [13]$$

where V_{p0} and V_{s0} represent the *P*- and *S*-wave velocity of the solid mantle, respectively, and dV is the reduction in the velocity, β is the ratio of the adiabatic bulk modulus (K_S) of the solid to the liquid, γ is the ratio of the shear modulus G to K_S for the solid mantle, and ρ_l and ρ_s are density of the melt phase and solid mantle, respectively. Λ_K and Λ_G are functions of melt geometry and can be approximated by (10)

$$\frac{K_b(F,\alpha)}{K_S} = 1 - F\Lambda_K(\alpha), \quad [14]$$

$$\frac{N(F,\alpha)}{G} = 1 - F\Lambda_G(\alpha), \quad [15]$$

where K_b and N are the bulk and shear modulus, respectively, of the solid skeleton, which are calculated at a given melt fraction F by replacing the regions containing liquid with empty pore spaces and the pore shape is described by the equivalent aspect ratio α (10). All the melt geometrical parameters (e.g., oblate spheroid model, equilibrium model, tube and crack model) can be converted to the equivalent aspect ratio. Λ_K and Λ_G, which are functions of α, are slopes of the normalized moduli $\frac{K_b}{K_S}$ and $\frac{N}{G}$ as a function of melt fraction F, respectively. They can be approximated as a liner function when F is relatively small (< ~10%). The slopes Λ_K and Λ_G for different melt geometries can be obtained from the Figs. 2 and 3 in Takei (10).

In order to assess which melt geometry is most applicable to realistic melts in the upper mantle, we have calculated the P-wave velocity reductions ($dlnV_p$) and S-wave velocity reductions ($dlnV_s$) for a partially molten assemblage consisting of San Carlos (SC) olivine (elastic data from Liu et al. (11)) plus various amount of dolomite or diopside melt as a function of the equivalent aspect ratio α (Fig. S7). The results were then compared with (1) experimentally determined relationship between velocity reduction and melt fraction by Chantel et al. (12) in a similar partially molten system (SC olivine + basaltic melt) at about 2.5 GPa, (2) well-constrained seismic velocity reductions for the upper mantle low-velocity zone (13–15), and (3) melt fractions in the low-velocity zone estimated from petrologic studies (16, 17) and space-time distribution of seamounts (18). For low-degree partial melts, the experimental results, seismic observations and petrologic melt fraction constraints can all be satisfied only when the melt aspect ratio (α) is about 0.01 (Fig. S7), which corresponds to the melt film geometry (10). In addition, carbonate melt has high wetting properties (19) and tends to form grain boundary thin films in olivine-carbonatite system (20). Thus, the melt film geometry with α = 0.01 is adopted in our following calculations for the velocities of melt-bearing mantle.

All the calculations were performed along a plausible mantle adiabatic temperature profile (21). We use the SC olivine data (11) as a representative for the solid mantle, since the elastic data for natural peridotite at simultaneous high pressure and high temperature conditions are not available. Most of the elastic data on peridotite are measured at high pressure but at room temperature (22), and their extrapolation to high temperature has significant uncertainty. Although the sound velocity of olivine is intrinsically different from peridotite, the relative changes in seismic properties due to the presence of melt should be comparable in both olivine and peridotite. The combination of V_P and V_S into the V_P/V_S ratio can be more sensitive to mantle physical state than the absolute V_P or V_S value alone (12). In addition, the major minerals in upper mantle show a relatively small range of V_P/V_S ratios (10) and the determined V_P/V_S ratio for natural peridotite at high pressures resembles that of olivine (22). We thus choose to use the V_P/V_S ratios calculated for the partially molten mantle analog (olivine + various amount of carbonate or silicate melt) as a function of depth for comparison with global radial seismic profiles in Fig. 3.

Text S4. *Comparison with previous results*

The density calculated using GGA from Desmaele et al. (21) is consistent with our GGA results, and their density data obtained by classical MD simulations are also in agreement with our experimental results (Fig. 2b). The fitting results for bulk modulus (K_{T0}) and its pressure derivative (K_T') also agree with each other within the uncertainties (Table 1). The classical MD simulations from Hurt (24), however, report a lower density for dolomite melt and a slightly different pressure dependence than our results and the results from Desmaele et al. (21). This may be because that the empirical potentials employed in Hurt (24) do not fully describe the behavior of dolomite melt. Using the empirical potentials developed by Hurt & Wolf (20), Hurt (24) reported an anomalous compression behavior for $MgCO_3$ melt with a surprisingly low density and high compressibility at low pressures compared to other carbonate melts. However, the anomalous behavior is not confirmed by our experimental measurements, at least not for $MgCO_3$-bearing dolomite melt. Comparison with the density of hydrous dolomite melt (with 10 wt% H_2O) measured recently by Ritter et al. (23) using X-ray absorption method (Fig. 2b) suggests that water can reduce the density of carbonate melt, thus increasing its buoyancy with the ambient mantle. Comparison with carbonated basaltic melt (with 5.0 wt% CO_2) (24) and carbonated $MgSiO_3$ melt (with 5.2 wt% CO_2) (25) suggests that pure carbonate melt is considerably lighter than carbonated silicate melt at the entire mantle conditions.

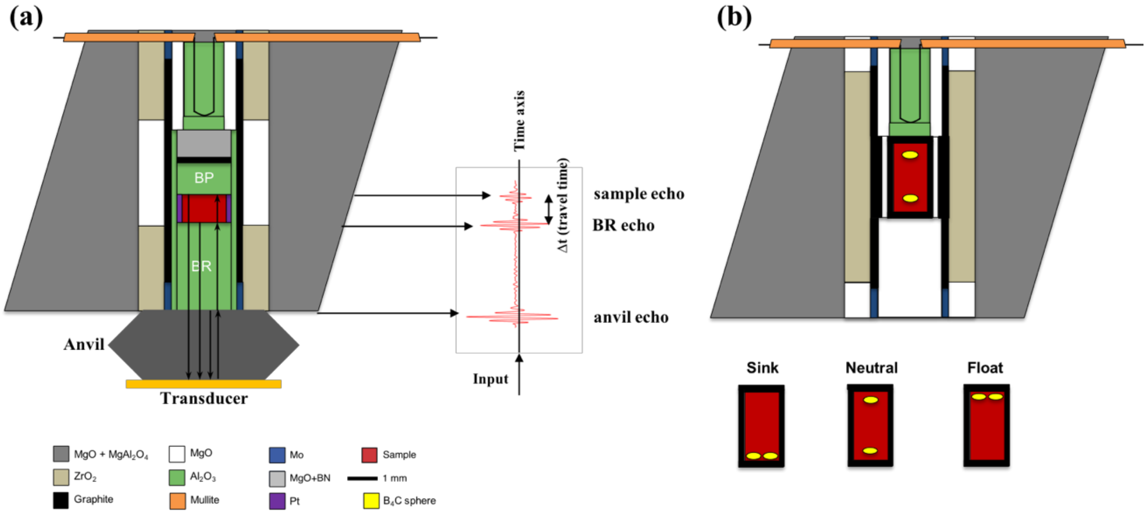

Fig. S1. (a) Cell assembly for ultrasonic experiments and a schematic drawing for travel time measurements. Black arrows indicate directions of sound waves in the cell. BR-buffer rod, BP-backing plate. (b) Cell assembly for sink-float density measurements and schematic drawings of sample capsules showing the sink, neutral, and float scenarios, respectively.

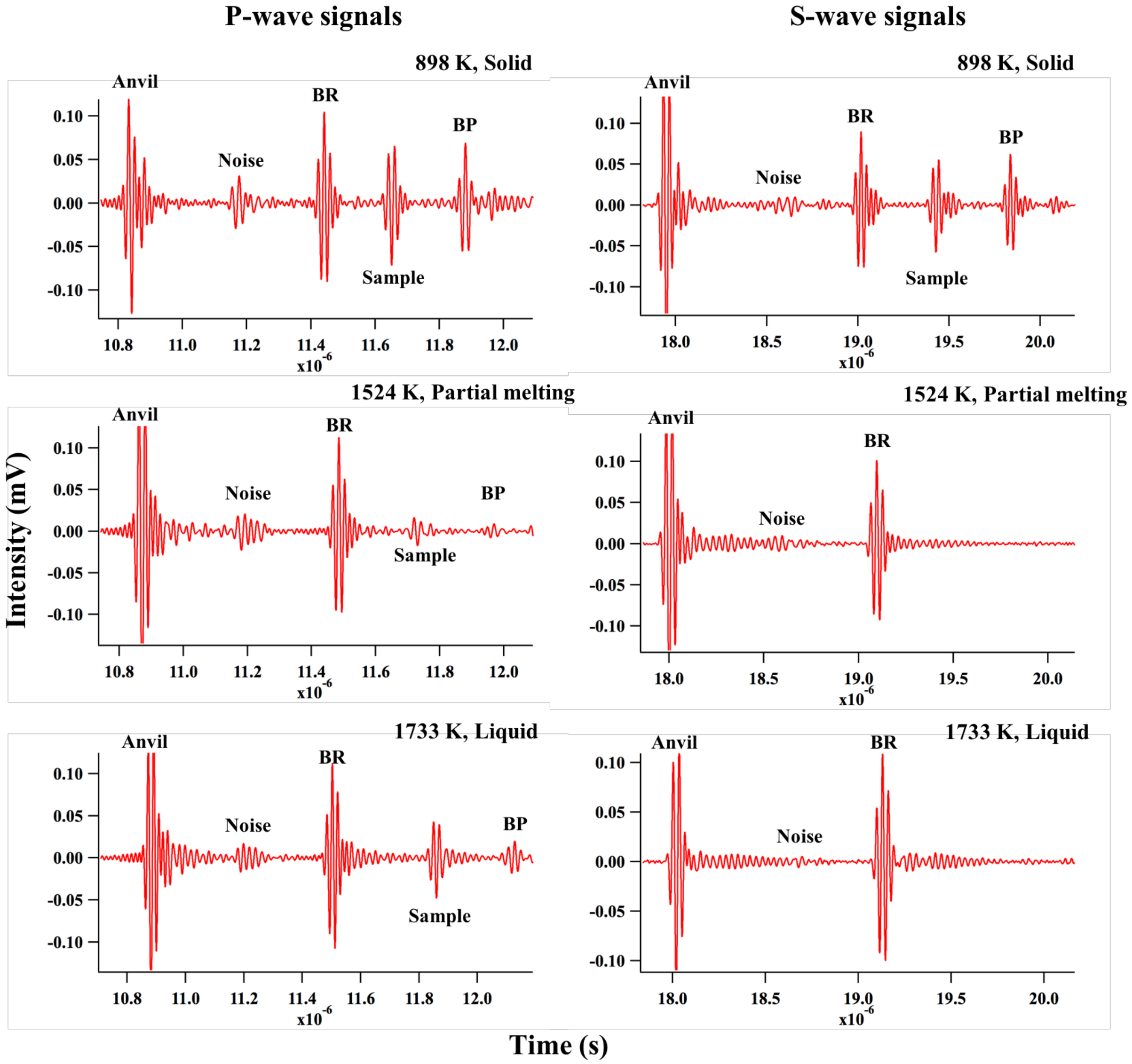

Fig. S2. Representative ultrasonic signals obtained for the dolomite sample at a constant load of 150 tons, showing the change of sample P- (left) and S-wave (right) signals with increasing temperature from the solid state (top), to the partially molten state (middle), and then to the fully molten state (bottom).

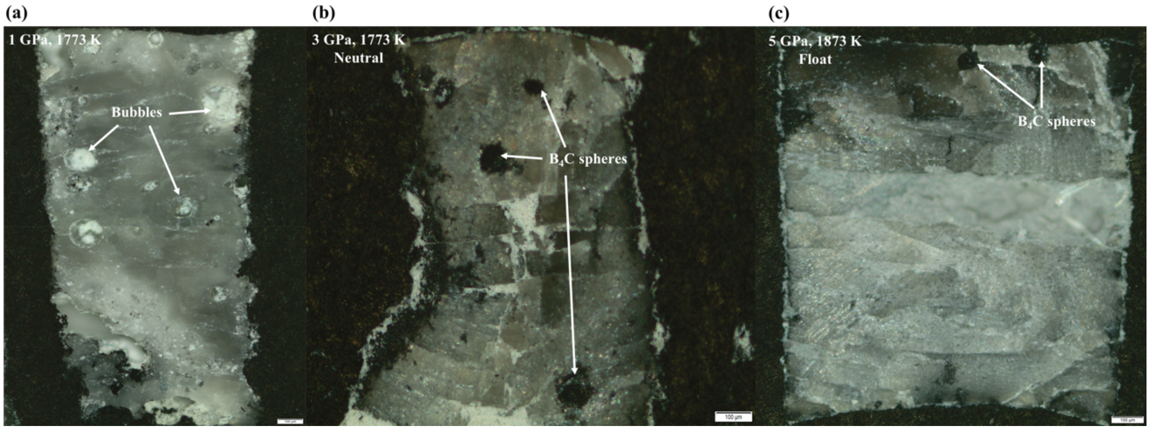

Fig. S3. Sink-float experimental results for dolomite melt. (a) The dolomite sample decomposes at 1 GPa and 1773 K, preventing the sinking of B_4C markers. (b) Neutral buoyancy of B_4C spheres in dolomite melt at 3 GPa and 1773 K. (c) Flotation of B_4C spheres in dolomite melt at 5 GPa and 1873 K.

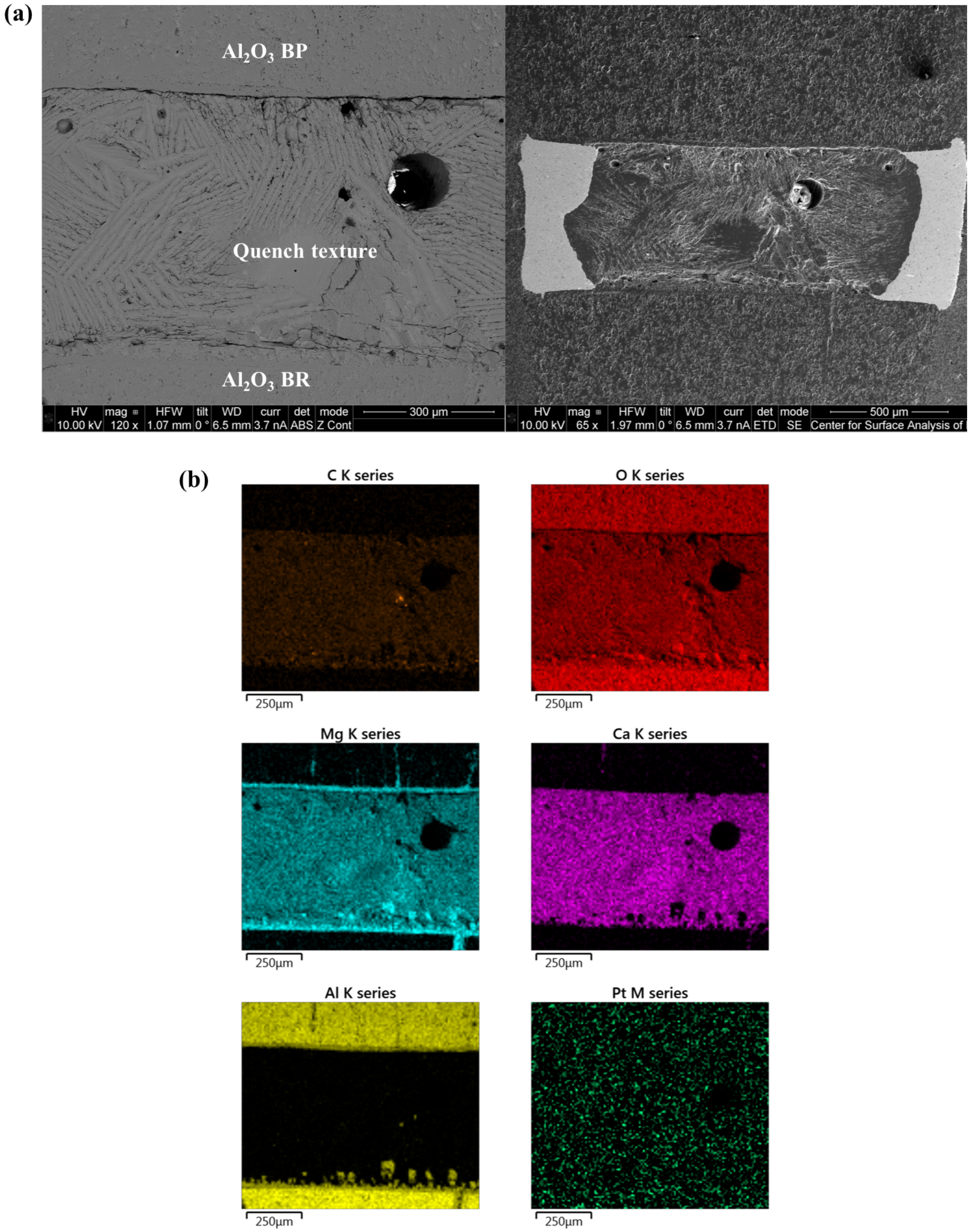

Fig. S4. (a) Backscattered electron (BSE) image (left) and secondary electron (SE) image of the quenched sample from ultrasonic measurements (T2261), BR-buffer rod, BP-backing plate. The sample shows the typical quench texture for carbonate melts, indicating that the sample was fully molten during the experiments. (b) Composition mapping of the quenched sample. At low pressures (<2.5 GPa), the dolomite melt sample may partly decompose to MgO plus a vapor phase. The MgO blobs then sank to the bottom of the liquid sample and reacted with Al_2O_3 buffer rod to form spinels. Due to the fact that velocity is a bulk property of a material, and most of the blobs are at the bottom of the sample, it is unlikely that they can affect the velocity results of the melt significantly.

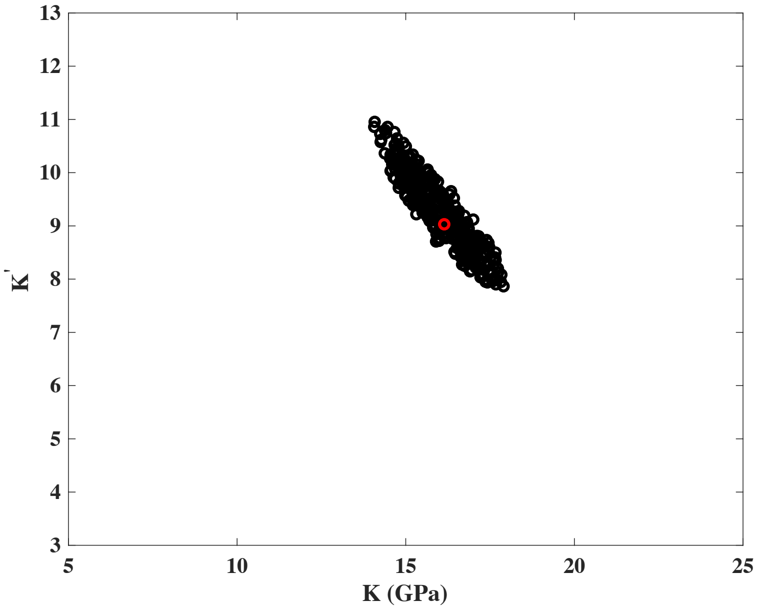

Fig. S5. Correlations between fitted K and K' for Birch-Murnaghan equation of state using the experimental velocity and density data.

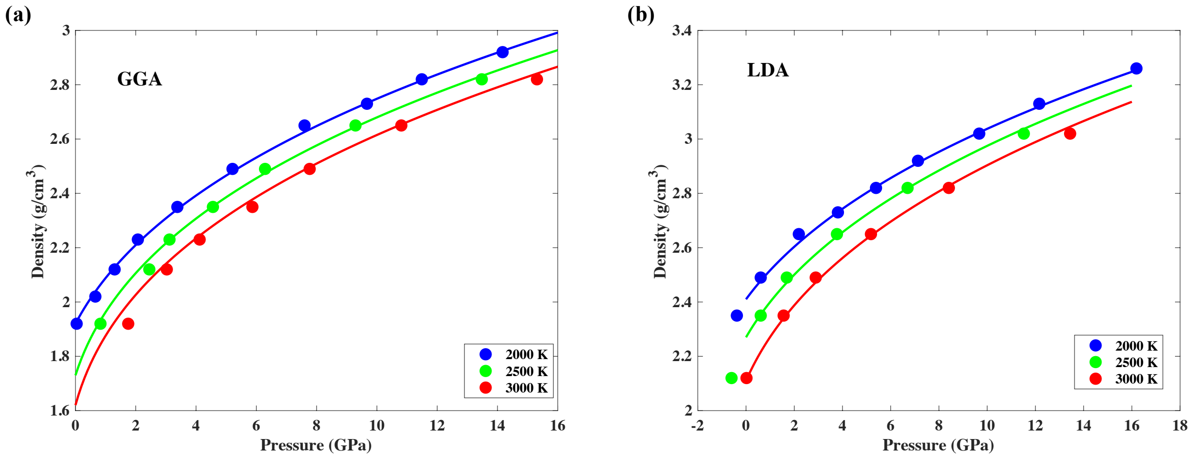

Fig. S6. FPMD simulation results for the density of dolomite melt based on (a) GGA and (b) LDA, respectively.

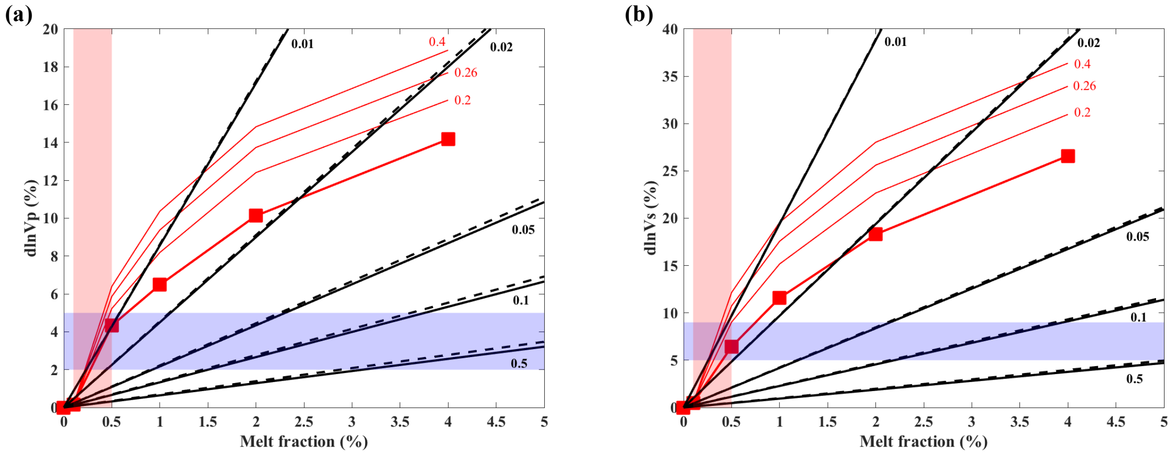

Fig. S7. (a) P-wave velocity reduction ($dlnV_p$) and (b) S-wave velocity reduction (dlV_s) as a function of melt fraction and equivalent aspect ratio α based on the model of Takei (10). Solid black lines-SC olivine + dolomite melt, dashed black lines-SC olivine + diopside melt and the numbers labelled are corresponding aspect ratio α. The data used for SC olivine is from Liu et al. (11). Red squares-experimental data from Chantel et al. (12) for SC olivine + basaltic melt and thin red lines-modeled results by correcting the anelastic effects expected for seismic waves using a range of values for the anelastic factor (See details in Chantel et al. (12)). Purple shaded areas-seismic velocity reductions observed for the low-velocity zone (13–15). Pink shaded areas-melt fractions for the low-velocity zone constrained from petrologic studies (16, 17) and space-time distribution of seamounts (18). For low-degree partial melts, the experimental results, seismic observations and petrologic constraints can only be satisfied when the melt aspect ratio α is ~0.01, corresponding to the melt film geometry.

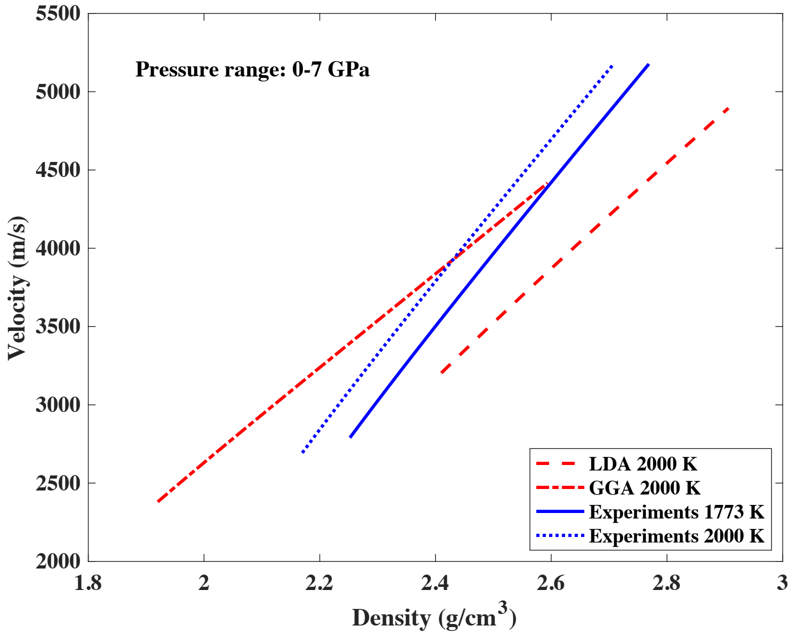

Fig. S8. Velocity-density relation for dolomite melt based on the fitting results from experiments, LDA, and GGA simulations, respectively. The different slopes between experimental curve and simulation curves are because that the fitted K' from experimental data is larger than the K' fitted from the simulation data (See Table 1). If a material follows the Birch's Law, then the velocity of the material should be a linear function of density regardless of the mechanisms (pressure or temperature) causing the changes in density. Our results show that the velocity-density relation for dolomite melt is temperature dependent, suggesting Birch's Law does not hold for dolomite melt, despite that velocity increases linearly with density. As velocity and density depend on pressure and temperature in different manners, the velocity-density plot may not be as informative as those plotted against pressure (Fig. 2) when determining the better techniques between LDA and GGA for velocity and density simulations. The velocity obtained from LDA at high pressures is at a similar range as that from experiments, but the density from LDA is higher than that obtained from experiments. Thus, in the velocity-density plot, the LDA curve shifts to the right of the experimental curve. While at the same pressure range, the velocity and density obtained from GGA are systematically lower than those from experiments. Therefore, the experimental result is closer to LDA at lower density but agrees better with GGA at higher density.

Table S1. Composition of the quenched samples measured by EDS (atomic %).

	T2207	T2208	T2261	T2262
C	22.33	19.51	19.37	20.65
O	57.42	58.62	61.16	59.52
Mg	7.48	9.59	8.81	9.17
Ca	12.52	11.91	10.50	10.43
Al	0.25	0.38	0.16	0.23
Pt	0	0	0	0

Table S2. Sound velocity data measured for dolomite melt.

Run#	P (GPa)	T (K)	Frequency (MHz)	Velocity c (m/s)	Average c (m/s)	s.d. (m/s)
T2207	2.14	1629	20	3871	3880	7
T2207	2.14	1629	25	3874		
T2207	2.14	1629	30	3878		
T2207	2.14	1629	40	3881		
T2207	2.14	1629	50	3884		
T2207	2.14	1629	60	3890		
T2207	1.96	1733	20	3836	3817	14
T2207	1.96	1733	25	3827		
T2207	1.96	1733	30	3824		
T2207	1.96	1733	40	3811		
T2207	1.96	1733	50	3805		
T2207	1.96	1733	60	3802		
T2207	1.91	1837	20	3786	3757	20
T2207	1.91	1837	25	3774		
T2207	1.91	1837	30	3761		
T2207	1.91	1837	40	3743		
T2207	1.91	1837	50	3740		
T2207	1.91	1837	60	3737		
T2207	1.82	1942	20	3653	3672	15
T2207	1.82	1942	25	3674		
T2207	1.82	1942	30	3686		
T2207	1.82	1942	40	3683		
T2207	1.82	1942	50	3653		
T2207	1.82	1942	60	3680		
T2208	1.39	1629	20	3732	3724	6
T2208	1.39	1629	25	3726		
T2208	1.39	1629	30	3721		
T2208	1.39	1629	40	3718		
T2208	1.39	1629	50	3723		
T2208	1.44	1733	20	3649	3643	6
T2208	1.44	1733	25	3646		
T2208	1.44	1733	30	3643		
T2208	1.44	1733	40	3643		
T2208	1.44	1733	50	3641		
T2208	1.44	1733	60	3633		
T2208	3.40	1629	20	4219	4226	8
T2208	3.40	1629	25	4227		
T2208	3.40	1629	30	4235		
T2208	3.40	1629	40	4231		
T2208	3.40	1629	50	4219		
T2261	2.43	1629	20	3904	3907	3
T2261	2.43	1629	25	3904		
T2261	2.43	1629	30	3904		
T2261	2.43	1629	40	3909		
T2261	2.43	1629	50	3909		
T2261	2.43	1629	60	3909		
T2261	2.05	1733	20	3888	3878	8
T2261	2.05	1733	25	3882		
T2261	2.05	1733	30	3883		
T2261	2.05	1733	40	3877		
T2261	2.05	1733	50	3872		
T2261	2.05	1733	60	3866		
T2261	1.96	1837	20	3865	3869	9

T2261	1.96	1837	25	3869		
T2261	1.96	1837	30	3869		
T2261	1.96	1837	40	3854		
T2261	1.96	1837	50	3872		
T2261	1.96	1837	60	3882		
T2262	3.23	1837	20	4121	4112	20
T2262	3.23	1837	25	4128		
T2262	3.23	1837	30	4130		
T2262	3.23	1837	40	4115		
T2262	3.23	1837	50	4099		
T2262	3.23	1837	60	4079		
T2262	4.46	1837	20	4517	4528	16
T2262	4.46	1837	25	4535		
T2262	4.46	1837	30	4552		
T2262	4.46	1837	40	4538		
T2262	4.46	1837	50	4517		
T2262	4.46	1837	60	4510		
T2439	2.08	1629	20	3825	3814	6
T2439	2.08	1629	25	3814		
T2439	2.08	1629	30	3809		
T2439	2.08	1629	40	3808		
T2439	2.08	1629	50	3813		
T2439	2.08	1629	60	3817		
T2439	1.64	1733	20	3749	3728	18
T2439	1.64	1733	25	3742		
T2439	1.64	1733	30	3734		
T2439	1.64	1733	40	3731		
T2439	1.64	1733	50	3701		
T2439	1.64	1733	60	3711		
T2439	2.97	1733	20	4278	4268	5
T2439	2.97	1733	25	4267		
T2439	2.97	1733	30	4267		
T2439	2.97	1733	40	4263		
T2439	2.97	1733	50	4265		
T2439	2.97	1733	60	4265		
T2439	2.36	1837	20	4033	4023	6
T2439	2.36	1837	25	4025		
T2439	2.36	1837	30	4019		
T2439	2.36	1837	40	4017		
T2439	2.36	1837	50	4021		
T2439	2.36	1837	60	4027		
T2439	4.11	1733	20	4611	4645	21
T2439	4.11	1733	25	4641		
T2439	4.11	1733	30	4639		
T2439	4.11	1733	40	4647		
T2439	4.11	1733	50	4664		
T2439	4.11	1733	60	4670		
T2439	4.19	1837	20	4632	4648	13
T2439	4.19	1837	25	4643		
T2439	4.19	1837	30	4641		
T2439	4.19	1837	40	4643		
T2439	4.19	1837	50	4660		
T2439	4.19	1837	60	4666		
T2439	4.52	1942	20	4557	4554	9
T2439	4.52	1942	25	4557		
T2439	4.52	1942	30	4562		

T2439	4.52	1942	40	4540		
T2439	5.88	1837	20	4928	4905	32
T2439	5.88	1837	25	4905		
T2439	5.88	1837	30	4888		
T2439	5.88	1837	40	4862		
T2439	5.88	1837	50	4942		
T2439	5.06	1942	20	4865	4856	18
T2439	5.06	1942	25	4868		
T2439	5.06	1942	30	4861		
T2439	5.06	1942	40	4830		
T2439	5.27	2046	20	4706	4701	7
T2439	5.27	2046	25	4697		

Table S3. FPMD simulation results for dolomite melt. Time refers to the simulation time.

V/Vx	Time (ps)	*V* (Å^3)	ρ (g/cm^3)	*T* (K)	E (eV)	σE, eV	*P* (GPa)	σP, GPa
GGA	*Vx =*	*1157.62 Å^3*						
1.1	27.33	1273.38	1.92	2000	-552.98	0.19	0.04	0.18
1.05	48.32	1215.50	2.02	2000	-553.01	0.21	0.66	0.11
1	56.34	1157.62	2.12	2000	-553.98	0.14	1.30	0.19
0.95	46.88	1099.74	2.23	2000	-554.22	0.13	2.07	0.12
0.9	55.16	1041.86	2.35	2000	-554.39	0.16	3.38	0.28
0.85	51.52	983.98	2.49	2000	-554.95	0.08	5.21	0.24
0.8	50.62	926.10	2.65	2000	-554.58	0.10	7.60	0.22
0.775	55.35	897.16	2.73	2000	-554.38	0.07	9.67	0.13
0.75	62.07	868.22	2.82	2000	-553.76	0.14	11.49	0.20
0.725	54.43	839.27	2.92	2000	-552.63	0.25	14.17	0.22
1.1	55.66	1273.38	1.92	2500	-544.39	0.24	0.83	0.11
1	55.97	1157.62	2.12	2500	-545.00	0.21	2.45	0.11
0.95	56.07	1099.74	2.23	2500	-547.15	0.29	3.12	0.17
0.9	55.22	1041.86	2.35	2500	-547.69	0.32	4.56	0.16
0.85	54.71	983.98	2.49	2500	-548.31	0.09	6.29	0.15
0.8	63.17	926.10	2.65	2500	-547.73	0.17	9.29	0.19
0.75	64.77	868.22	2.82	2500	-546.97	0.15	13.48	0.17
1.1	79.64	1273.38	1.92	3000	-534.57	0.27	1.75	0.14
1	85.25	1157.62	2.12	3000	-538.31	0.33	3.03	0.09
0.95	69.51	1099.74	2.23	3000	-539.19	0.32	4.12	0.14
0.9	84.13	1041.86	2.35	3000	-540.56	0.59	5.87	0.18
0.85	83.50	983.98	2.49	3000	-541.01	0.31	7.77	0.16
0.8	82.60	926.10	2.65	3000	-540.53	0.44	10.81	0.16
0.75	87.77	868.22	2.82	3000	-538.89	0.43	15.31	0.26
LDA	*Vx =*	*1157.62 Å^3*						
0.9	52.57	1041.86	2.35	2000	-612.62	0.07	-0.38	0.14
0.85	59.40	983.98	2.49	2000	-613.76	0.10	0.61	0.15
0.8	58.57	926.10	2.65	2000	-615.04	0.08	2.19	0.16
0.775	48.92	897.16	2.73	2000	-615.31	0.09	3.81	0.12
0.75	31.00	868.22	2.82	2000	-615.55	0.16	5.39	0.19
0.725	58.49	839.27	2.92	2000	-615.70	0.17	7.13	0.89
0.7	68.33	810.33	3.02	2000	-615.52	0.14	9.67	0.23
0.675	65.09	781.39	3.13	2000	-615.25	0.18	12.16	0.24
0.65	64.87	752.45	3.26	2000	-614.30	0.16	16.19	0.21
0.9	51.52	1041.86	2.35	2300	-608.38	0.26	0.21	0.15
0.85	50.62	983.98	2.49	2300	-609.81	0.14	1.42	0.13
0.8	62.07	926.10	2.65	2300	-610.85	0.12	3.30	0.14
0.75	55.66	868.22	2.82	2300	-611.64	0.11	6.19	0.19
0.7	55.97	810.33	3.02	2300	-611.53	0.11	10.85	0.16
1	60.65	1157.62	2.12	2500	-602.93	0.32	-0.60	0.16
0.9	58.27	1041.86	2.35	2500	-606.34	0.14	0.61	0.14
0.85	50.72	983.98	2.49	2500	-607.53	0.08	1.69	0.08
0.8	56.56	926.10	2.65	2500	-608.58	0.12	3.77	0.16
0.75	60.06	868.22	2.82	2500	-609.37	0.13	6.70	0.12
0.7	66.16	810.33	3.02	2500	-608.94	0.09	11.52	0.15
1	56.07	1157.62	2.12	2600	-602.30	0.20	-0.50	0.15
0.9	55.22	1041.86	2.35	2600	-603.11	0.28	1.03	0.18
0.85	54.71	983.98	2.49	2600	-605.43	0.36	2.17	0.21
0.8	63.17	926.10	2.65	2600	-607.24	0.14	4.05	0.28
0.75	64.77	868.22	2.82	2600	-607.98	0.34	7.22	0.26
0.7	79.64	810.33	3.02	2600	-607.82	0.11	11.86	0.24
1	85.25	1157.62	2.12	3000	-592.89	0.53	0.02	0.21

0.9	69.51	1041.86	2.35	3000	-598.21	0.81	1.56	0.15
0.85	84.13	983.98	2.49	3000	-600.90	0.19	2.89	0.27
0.8	83.50	926.10	2.65	3000	-601.23	0.43	5.18	0.16
0.75	82.60	868.22	2.82	3000	-602.94	0.32	8.41	0.21
0.7	87.77	810.33	3.02	3000	-601.99	0.42	13.44	0.22

References

1. F. Birch, Elasticity and constitution of the Earth's interior. *J. Geophys. Res.* **57**, 227–286 (1952).
2. O. L. Anderson, *Equations of State of Solids for Geophysics and Ceramic Science* (Oxford University Press, 1995).
3. S. M. Hurt, R. A. Lange, The density of Li_2CO_3-Na_2CO_3-K_2CO_3-Rb_2CO_3-Cs_2CO_3-$CaCO_3$-$SrCO_3$-$BaCO_3$ liquids: New measurements, ideal mixing, and systematic trends with composition. *Geochim. Cosmochim. Acta* **248**, 123–137 (2019).
4. F. D. Stacey, High pressure equations of state and planetary interiors. *Reports Prog. Phys.* **68**, 341–383 (2005).
5. L. Stixrude, N. de Koker, N. Sun, M. Mookherjee, B. B. Karki, Thermodynamics of silicate liquids in the deep Earth. *Earth Planet. Sci. Lett.* **278**, 226–232 (2009).
6. P. D. Asimow, T. J. Ahrens, Shock compression of liquid silicates to 125 GPa: The anorthite-diopside join. *J. Geophys. Res. Solid Earth* **115** (2010).
7. M. Xu, *et al.*, Ultrasonic Velocity of Diopside Liquid at High Pressure and Temperature: Constraints on Velocity Reduction in the Upper Mantle Due to Partial Melts. *J. Geophys. Res. Solid Earth* **123**, 8676–8690 (2018).
8. E. Desmaele, N. Sator, R. Vuilleumier, B. Guillot, The $MgCO_3$-$CaCO_3$-Li_2CO_3-Na_2CO_3-K_2CO_3 melts: Thermodynamics and transport properties by atomistic simulations. *J. Chem. Phys.* **150**, 214503 (2019).
9. A. N. Clark, C. E. Lesher, Elastic properties of silicate melts: Implications for low velocity zones at the lithosphere-asthenosphere boundary. *Sci. Adv.* **3**, e1701312 (2017).
10. Y. Takei, Effect of pore geometry on V_P/V_S: From equilibrium geometry to crack. *J. Geophys. Res.* **107**, 2043 (2002).
11. W. Liu, J. Kung, B. Li, Elasticity of San Carlos olivine to 8 GPa and 1073 K. *Geophys. Res. Lett.* **32**, L16301 (2005).
12. J. Chantel, *et al.*, Experimental evidence supports mantle partial melting in the asthenosphere. *Sci. Adv.* **2**, e1600246 (2016).
13. H. Kawakatsu, *et al.*, Seismic evidence for sharp litosphere-astenosphere boundaries of oceanic plates. *Science.* **324**, 499–502 (2009).
14. C. A. Rychert, P. M. Shearer, A Global View of the Lithosphere-Asthenosphere

Boundary. *Science.* **324**, 495–498 (2009).

15. K. M. Fischer, H. A. Ford, D. L. Abt, C. A. Rychert, The Lithosphere-Asthenosphere Boundary. *Annu. Rev. Earth Planet. Sci.* **38**, 551–575 (2010).
16. M. M. Hirschmann, Partial melt in the oceanic low velocity zone. *Phys. Earth Planet. Inter.* **179**, 60–71 (2010).
17. D. C. Presnall, G. H. Gudfinnsson, Carbonate-rich melts in the oceanic low-velocity zone and deep mantle. *Geol. Soc. Am. Spec. Pap.* **388**, 207–216 (2005).
18. C. P. Conrad, K. Selway, M. M. Hirschmann, M. D. Ballmer, P. Wessel, Constraints on volumes and patterns of asthenospheric melt from the space-time distribution of seamounts. *Geophys. Res. Lett.* **44**, 7203–7210 (2017).
19. W. G. Minarik, E. B. Watson, Interconnectivity of carbonate melt at low melt fraction. *Earth Planet. Sci. Lett.* **133**, 423–437 (1995).
20. T. Yoshino, M. Laumonier, E. Mcisaac, T. Katsura, Electrical conductivity of basaltic and carbonatite melt-bearing peridotites at high pressures: Implications for melt distribution and melt fraction in the upper mantle. *Earth Planet. Sci. Lett.* **295**, 593–602 (2010).
21. T. Katsura, A. Yoneda, D. Yamazaki, T. Yoshino, E. Ito, Adiabatic temperature profile in the mantle. *Phys. Earth Planet. Inter.* **183**, 212–218 (2010).
22. X. Wang, T. Chen, Y. Zou, R. C. Liebermann, B. Li, Elastic wave velocities of peridotite KLB-1 at mantle pressures and implications for mantle velocity modeling. *Geophys. Res. Lett.* **41**, 3289–3297 (2015).
23. X. Ritter, *et al.*, Density of hydrous carbonate melts under pressure, compressibility of volatiles and implications for carbonate melt mobility in the upper mantle. *Earth Planet. Sci. Lett.* **533**, 116043 (2020).
24. S. Ghosh, E. Ohtani, K. Litasov, A. Suzuki, T. Sakamaki, Stability of carbonated magmas at the base of the Earth's upper mantle. *Geophys. Res. Lett.* **34**, L22312 (2007).
25. D. B. Ghosh, S. K. Bajgain, M. Mookherjee, B. B. Karki, Carbon-bearing silicate melt at deep mantle conditions. *Sci. Rep.* **7**, 1–8 (2017).